Research Article | Vol. 29, No. 12 / 7 June 2021 / Optics Express 17915
Optics EXPRESS

Simultaneous measurement of temperature and curvature using ring-core fiber-based Mach-Zehnder interferometer

WEIHAO YUAN,[1] QIANCHENG ZHAO,[1,*] LINGDUO LI,[2] YU WANG,[1] AND CHANGYUAN YU[1]

[1] *Photonic Research Centre, Department of Electronic and Information Engineering, The Hong Kong Polytechnic University, Hong Kong SAR, China*
[2] *Photonics Research Centre, Shenzhen Research Institute of The Hong Kong Polytechnic University, Shenzhen, China*
[*] *Qiancheng.zhao@polyu.edu.hk*

Abstract: In this paper, the Mach-Zehnder interferometer (MZI) based on ring-core fiber was proposed and manufactured. Benefiting from the identical diameters of ring-core fiber, no-core fiber, and single-mode fiber, the MZI fiber sensor can be prototyped by sandwiching the ring-core fiber between the no-core fiber and the single-mode fiber (SMF). With the proposed specific structure of the ring-core fiber, the simultaneous measurement of temperature and curvature was achieved with the MZI sensor by means of monitoring the wavelength shift of interference dips. Experimental results have shown that the sensitivity of curvature sensing could reach up to -3.68 nm/m^{-1} in the range from 1.3856 m^{-1} to 3.6661 m^{-1} with high linearity of 0.9959. Meanwhile, the maximum temperature sensitivity is measured to be 72 pm/$^{\circ}C$ with a fairly good linearity response of 0.9975. In addition, by utilizing the 2×2 matrix algorithm, the dual demodulation of temperature and curvature can be readily realized for the purpose of direct sensing. It is believed that the proposed special structure-based MZI sensor may show great potential applications in the field of fiber-optics sensing and structural health monitoring (SHM).

1. Introduction

Fiber-optic sensors have attracted enormous attention since the late 1970s due to their superior and incomparable advantages, such as cost-efficient, easy-fabrication, high sensitivity, chemically-inert and immune to electromagnetic irradiation. A large number of applications based on fiber-optic sensors have been developed including the sensing of temperature [1,2], strain [3,4], curvature [5,6], refractive index (RI) [7,8], pH value [9,10], humidity [11,12] and gas [13,14]. Among these parametric sensors, it has been shown that curvature is one of the most important physical parameters because it greatly impacts practical applications including infrastructure health monitoring and astrophysics. To date, a variety of specialized optical fiber structures have been created for curvature sensing. For instance, in 2017, Tian et al. reported a twisted single-mode–multimode–single-mode hybrid fiber structure with a curvature sensitivity of -2.42 nm/m^{-1} over the measurement range of 0-1.7390 m^{-1} [15]. Following his work, Dong *et al.* proposed the cascaded fiber interferometer with a sensitivity of 4.362 nm/m^{-1} in the measurement range of 0-1.134 m^{-1} [5]. Jiang et al. reported the Mach-Zehnder interferometer (MZI) based on D-Shaped Fiber Grating and achieved the sensitivity up to 87.7 nm/m^{-1} to the low sensing range from 0 to 0.3 m^{-1} [16]. Barrera et al. used the Long Period Gratings (LPG) in multicore fibers and realized the linear sensing from 0 to 1.77 m^{-1} with the sensitivity up to -4.85 nm/m^{-1} [17]. Extensive research has manifested that fiber-optic sensors are very susceptible to the surrounding environment, especially the temperature. The change of temperature can influence the interference patterns of input optical signals severely, which in turn leads to the

#425580 https://doi.org/10.1364/OE.425580
Journal © 2021 Received 19 Mar 2021; revised 18 May 2021; accepted 19 May 2021; published 25 May 2021

Optics EXPRESS

inevitable measurement error in the course of curvature sensing. Therefore, the simultaneous monitoring of temperature and curvature is of great importance for the widespread applications of multiparametric fiber-optic sensors with reduced environmental errors and high-precision experimental results.

In view of this, herein, we firstly proposed the ring-core fiber (RCF)-based MZI fiber-optic sensor for the simultaneous measurement of temperature and curvature. The MZI sensor consists of two segments of single mode fiber (SMF), 1-mm no core fiber (NCF), and 20-mm RCF. Benefiting from the identical fiber diameters of SMF, NCF, and RCF, the sensor can be fabricated by direct fusion splicing which indicates the relatively stronger structure compared to thin-tapered or side-polished fiber structure and simplified preparation method compared to LPG sensor or specifically structured fiber. The utilization of NCF between SMF and RCF can not only excite multiple cladding modes in RCF directly, but also features the self-contained structure with the easy-to-fabricate advantage. The proposed MZI sensor shows good curvature sensitivity of up to -3.68 nm/m^{-1} with a relatively large measurement range from 1.3856 m^{-1} to 3.6661 m^{-1}. The linearities of curvature increasing and decreasing reach 0.9924 and 0.9959 which demonstrates the repeatable and reliable sensing performance. In addition, the temperature sensing was also studied and the experimental results presented the maximum sensitivity of 72 pm/°C with the linearity of 0.9975.

2. Experiments and principle

The NCF and RCF used in the MZI sensor were fabricated by the Yangtze Optical Fibre Company (YOFC) and the commercially standard SMFs (SMF-28, Corning) were used for laser coupling in and out of the MZI structure. The microscope images of cross sections of the NCF and RCF are shown in Fig. 1. The diameters of NCF and RCF are measured to be the same (d ~125 μm), which enables the direct fusion splicing of NCF, RCF, and SMF without mode mismatching. The RCF is comprised of three main parts: the fiber center (FC), ring core (RC), and cladding area. The refractive index (RI) of the FC and cladding part is the same with a value of 1.44402, while the RI of RC is 0.93% higher. The diameters of FC and RC are measured as 10.9 μm and 18.7 μm, respectively.

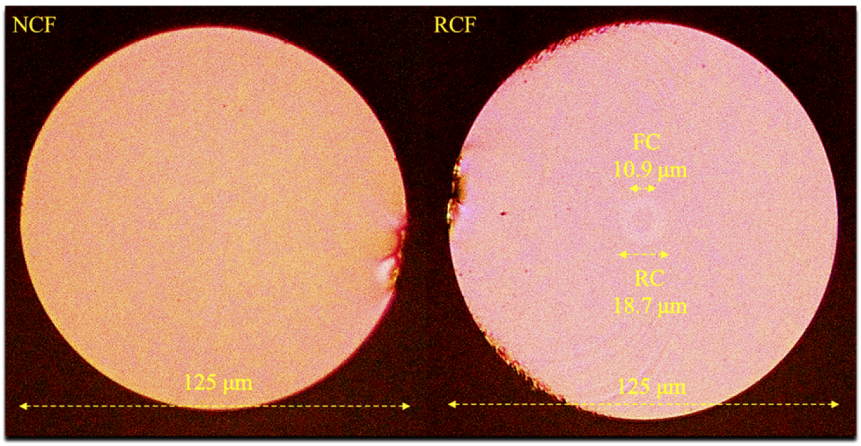

Fig. 1. Microscope images of section views of NCF and RCF.

The schematic diagrams of the experimental setup depicting the MZI sensor structure are shown in Figs. 2(a) and 2(b). The MZI sensor is primarily formed by fusion splicing 1-mm NCF with 20-mm RCF (N-R fiber structure), which is followed by the further connection of the N-R

Optics EXPRESS

fiber structure with two segments of SMFs. The MZI sensor is held by two fiber holders which are fixed on the translation stations. One of the stations is immobilized and the other one can be tuned through the rotary controller. The distance between two fiber holders (L_0) is set to be 50 mm to enable a relatively large sensing range with the moving step of 10 μm. The SMF fusion spliced with the NCF is connected to a broadband light source (BBS) with spectral coverage from 1470 to 1670 nm. The output light of BBS can be coupled into the optical spectrum analyzer (OSA, YOKOGAWA, AQ6370D) with a resolution of 0.02 nm via the transmission of SMF connected to the RCF.

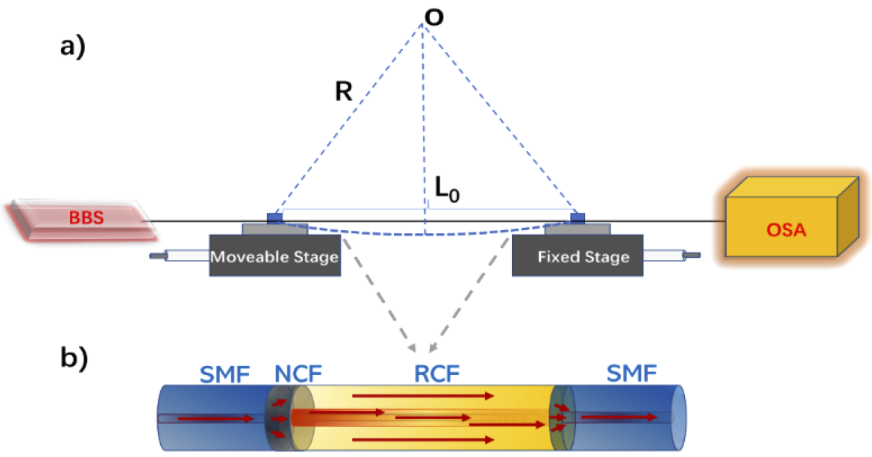

Fig. 2. (a) Schematic diagrams of the experimental setup for curvature sensing. (b) Illustration of MZI sensor based on the ring core fiber.

Different curvature values can be achieved by moving the translation stage with a step of 10 μm. In general, the curvature can be calculated by the equation shown below [18]:

$$c = \frac{1}{R} \cong \sqrt{\frac{24x}{{L_0}^3}} \tag{1}$$

where C refers to the curvature value, R represents the bending radius, x is the displacement of the moveable stage, and L_0 is the fiber length between two fiber holders when the fiber is straight.

Intensive studies have shown that the interference pattern of the MZI structure is varied with the differences of different MZI arms. The discrepancy of arm's length and effective RIs are closely associated with the generation of the interference patterns. For the MZI sensor proposed in this paper, the physical lengths of the core arm and cladding arm are the same, indicating that the generation of the interference pattern is caused by the effective RI difference between the fiber core and cladding. As a result, the intensity of the output light can be expressed by the following equation below:

$$I = I_1 + \sum\nolimits_k I_2^k + \sum\nolimits_m 2 \cdot \sqrt{I_1 \cdot I_2^k} \cos\left[\frac{2\pi}{\lambda} \cdot (n_{eff}^1 - n_{eff}^{2,k}) \cdot L\right] \tag{2}$$

where I represents the intensity of output light, and I_1 is the intensity of RC mode. I_2^k shows the intensity of FC mode and multiple cladding modes. Accordingly, the effective RI of the RC mode, and the FC and multiple cladding modes are expressed as n_{eff}^1 and $n_{\text{eff}}^{2,k}$. L represents the interference length of the MZI structure.

Optics EXPRESS

In line with the principles demonstrated in [19], the relationship between the wavelength of interference dip and bending curvature can be expressed as:

$$\lambda_{\mathrm{dip}} = \frac{\Delta n_{\mathrm{eff}} L}{2m+1} + \frac{\mathrm{k}\cdot\mathrm{L}\cdot\mathrm{s}}{2m+1} \times C \tag{3}$$

where m is an integer, k is the constant of the strain RI coefficient. L is the interference length. s is the distance between the core mode and cladding modes, C is the bending curvature and Δn_{eff} is the effective RI difference between the core and cladding modes. According to Eq. (3), the dip wavelength is linearly proportional to the bending curvature with a slope coefficient described as $\frac{\mathrm{kLs}}{2m+1}$. Because of the negative strain RI coefficient [20], the wavelength of interference dip will induce blueshift with the increase of bending curvature.

In addition to the bending curvature, it should be noted that the temperature variation can also give rise to the shift of interference dip. The dip wavelength of the destructive interference can be calculated by the following equations [5,12]:

$$2\pi \cdot (n_{\mathrm{eff}}^{1} - n_{\mathrm{eff}}^{2,k}) \cdot L/\lambda = (2m+1)\pi \tag{4}$$

$$\lambda_{\mathrm{dip}} = \frac{2\Delta\, n_{\mathrm{eff}} L}{2m+1} = \frac{2(\Delta n_{\mathrm{eff}} + \vartheta \Delta T)\,(L_0 + k_0 \Delta T)}{2m+1} \tag{5}$$

Δn_{eff} refers to the effective RI difference between the RC mode with the FC and the cladding modes. λ_{dip} means the wavelength of the interference dip. L_0 is the initial interference length of the MZI at room temperature (RT, 25°C). ϑ represents the difference of thermo-optic coefficient between the core and cladding. k_0 represents the thermal expansion coefficient of the RCF and ΔT is the temperature variation. The change of temperature will result in two main changes of the MZI sensor. The first change is the thermo-optic coefficient which determines the variation of the effective RI difference between core and cladding, while the second one is the thermal expansion coefficient that affects the MZI interference length. Due to the fact that the change of L induced by thermal effect is usually very small and the change of the interference spectra is negligible, it is apparent that the thermal response on the MZI sensor is mainly attributed to the thermo-optic coefficient which leads to the change of Δn_{eff}. According to Eq. (5), the relationship of dip wavelength and temperature depends on the coefficient $\frac{2L\vartheta}{2m+1}$, which can be regarded as a constant. Therefore, the above theoretical derivation indicates the linear dependence of dip wavelength on the change of temperature.

The effect of the length of NCF and RCF on the MZI interference patterns is firstly studied, and the results are shown in Fig. 3. As seen from Fig. 3(a), 1-mm NCF is applied in the MZI structure and connected to RCF with varying lengths of 10 cm, 6.7 cm, 4.3 cm, 2.5 cm, 2 cm, 1.5 cm, 1 cm, and 0.5 cm. It is seen that the extinction ratio (ER) is very small when 10 cm RCF is used, which can be attributed to the dispersion of the excited cladding modes. With the decrease of RCF length, the ER is increased and the free spectral range (FSR) is broadened. Based on the experimental results, a short section of RCF (L ~2 cm) is chosen for a relatively large FSR and long interference distance for curvature sensing. Figure 3(b) illustrates the interference spectra of 2 cm RCF-based MZI with different lengths of NCF at 10 mm, 7 mm, 5 mm, 3 mm, 1 mm, and 0, respectively. The longest NCF (L ~10 cm) used in our experiments results in a small ER due to the large transmission loss in NCF. With the decrease of NCF length, the ER is increased accordingly. However, it is noticed that the ER of interference pattern becomes negligible without the NCF (0-mm NCF). This is because no adequate cladding modes can be excited. On the basis of all the collected results, 1-mm NCF and 2-cm RCF are selected to construct the MZI sensor with the proposed SMF-NCF-RCF-SMF structure.

Firstly, the performance of light transmission in the straight RCF and bent RCF with the curvature of around 1.3856 m^{-1} are computationally simulated, as shown in Figs. 4(a) and 4(b). The MZI modeling in the natural (straight) and curved states with SMF-NCF-RCF-SMF are

Optics EXPRESS

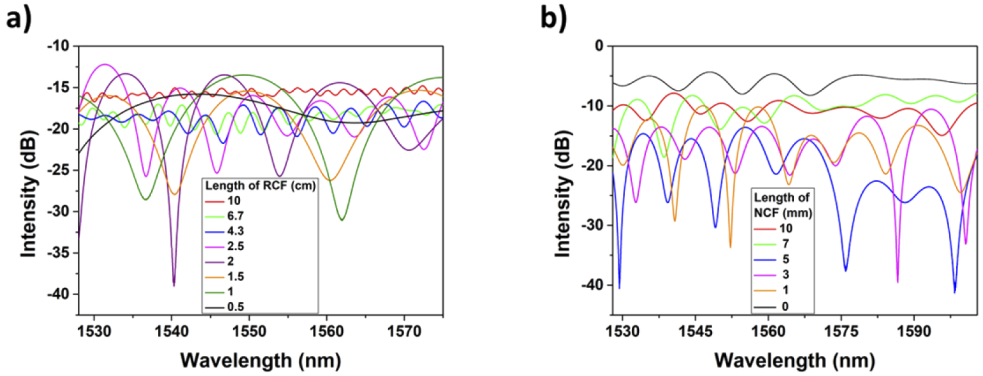

Fig. 3. (a) Interference spectra of 1-mm NCF MZI sensor with different lengths of RCF at 10 cm, 6.7 cm, 4.3 cm, 2.5 cm, 2 cm, 1.5 cm, 1 cm, and 0.5 cm and that of (b) 2-cm RCF MZI sensor with different lengths of NCF at 10 mm, 7 mm, 5 mm, 3 mm, 1 mm and 0.

conducted using Rsoft with the Beam PROP function. For SMF, the diameters of core and cladding are set to be 9 μm and 125 μm with the RI values of 1.4504 and 1.4447, respectively. The lengths of NCF and RCF are set as 1 mm and 20 mm. The geometry of the RCF is modeled based on the aforementioned designed parameters [Fig. 1(b)]. The incident wavelength is selected as 1550 nm as the free-space wavelength.

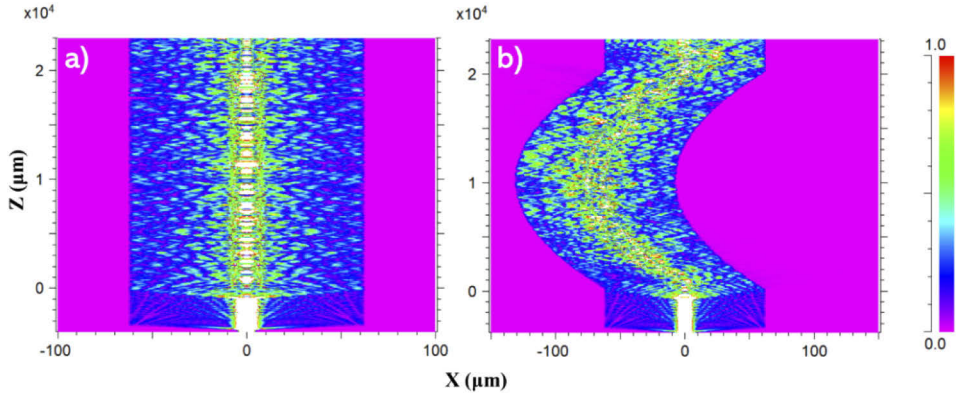

Fig. 4. Rsoft simulation results of light transmission in (a) straight RCF and (b) curved RCF.

Further to the light transmission properties of the RCF in different statuses, the mode distributions of the cross-section region of the RCF are also simulated and shown in Fig. 5. Figures 5(a)-(c) display the mode profiles of the cross-section region of the straight RCF at different transmission distances of 1 mm, 10 mm, and 20 mm, respectively. It can be clearly seen that different fiber modes, including RC mode, FC mode, and cladding modes, are excited and interfere in the RCF and then coupled into the SMF. Due to the specific layout of the ring-core structure, these fiber modes can be fairly sensitive to bending, indicating that a slight curvature value will result in significant variation of fiber modes. Accordingly, the mode profiles of the cross-section region of the bent RCF at different transmission distances are also simulated, as illustrated in Figs. 5(d)-(f). It is seen that the curvature-induced change in the fiber modes directly results in the change of interference patterns of the RCF.

Optics EXPRESS

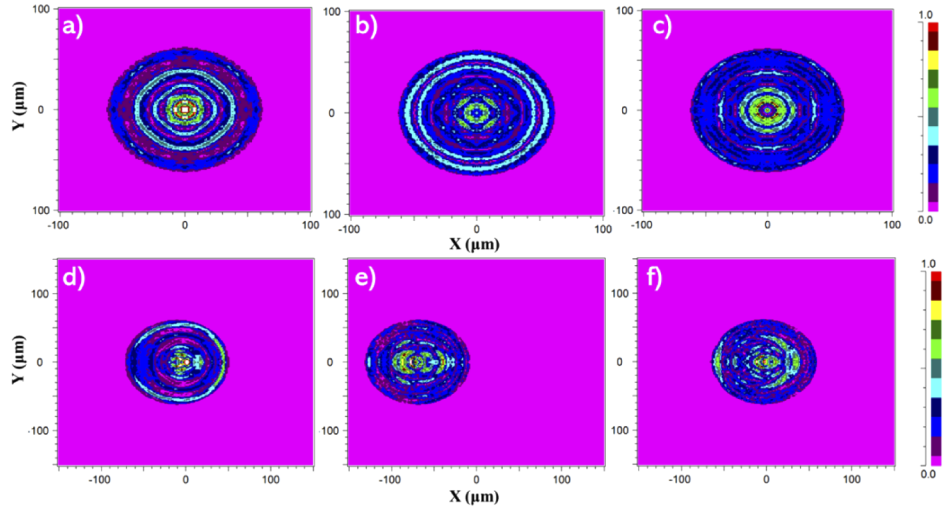

Fig. 5. Simulated mode distribution of the cross-section region of the straight RCF with the transmission distance of (a) 1 mm, (b) 10 mm, (c) 20 mm, and that of the curved RCF with the transmission distances of (d) 1 mm, (e) 10 mm, and (f) 20 mm.

3. Analysis and discussion

The experiment on curvature sensing using the RCF-based MZI fiber structure has been performed and the results are shown in Fig. 6. The optical spectrum is collected in the range of 1575-1645 nm, and it is seen that five interference dips are observed in the measurement range. The degree of curvature is altered by turning the rotator-driven translation stage with the step of 10 μm and the interference pattern is monitored and saved for comparison by the OSA at different steps. Different curvature values are recorded as 1.3856 m^{-1}, 1.9596 m^{-1}, 2.4 m^{-1}, 2.7713 m^{-1}, 3.0984 m^{-1}, 3.3941 m^{-1}, 3.6661 m^{-1}. As can be seen from Fig. 6, with the increase of the curvature value, the wavelength of the interference dip reveals a continuous blue shift, which is in good agreement with the theoretical analysis. To realize the dual demodulation of temperature and curvature, two characteristic interference dips are chosen for analysis. The first interference dip around 1587 nm is named dip 1, and the second one around 1642 nm is denoted as dip 2.

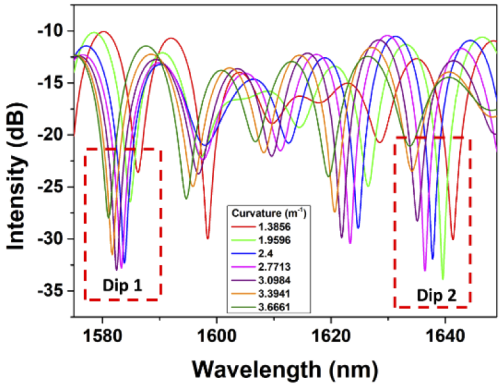

Fig. 6. Interference spectra of the MZI fiber sensor with different bending curvatures.

Optics EXPRESS

The detailed interference spectra of dip 1 are displayed in Fig. 7(a) and the relationship between the curvature and the dip wavelength is plotted in Fig. 7(b). The increasing and decreasing curvature are realized by turning the rotator-driven movable translation stage. For dip 1, with the increase of the curvature value, the dip wavelength presents a linear blue shift. The sensitivity is calculated to be -2.21 nm/m^{-1} with high linearity of 0.9961. In contrast, the decrease of curvature gives rise to the redshift of dip wavelength. The slope is fit as -2.33 nm/m^{-1} with the adjusted R-square value of 0.9969, which indicates the highly linear dependence of dip wavelength on the curvature value. Similarly, the wavelength of dip 2 also demonstrates the blue shift trend with the increase of curvature [Fig. 8(a)]. However, in terms of the featured dip 2, a higher sensitivity of -3.48 nm/m^{-1} is achieved with the increase of curvature. The good linearity is also measured with a high R-square value of 0.9924. With the decrease of the curvature, the sensitivity is also as high as -3.68 nm/m^{-1} with a high R-square value of 0.9959. From the experimental results, it is seen that the maximum curvature sensitivity can reach up to -3.68 nm/m^{-1}, which is around 1.5 times larger than the results reported in [15,21].

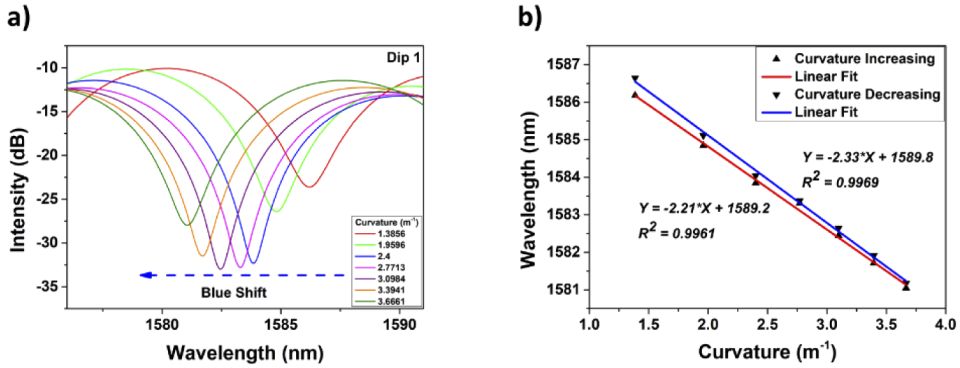

Fig. 7. (a) Interference spectra of dip 1 with different curvature. (b) Relationship between curvature and dip wavelength with curvature increasing and decreasing.

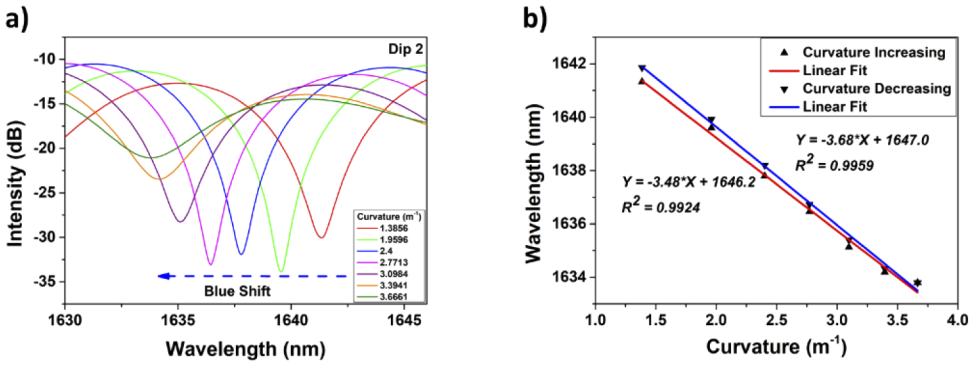

Fig. 8. (a) Interference spectra of dip 2 with different curvature and the (b) relationship between curvature and dip wavelength with curvature increasing and decreasing (b).

Finally, the experiments on temperature sensing are also conducted and the results are presented in Figs. 9(a) and 9(b). The interference spectra of dip 1 are displayed in Figs. 9(a) and Fig. 9(b) presents that of dip 2. According to Eq. (5), the relationship between the dip wavelength and temperature depends on the factor $\frac{2L\vartheta}{2m+1}$, which is a positive constant. Thus, with the increase of temperature, the dip wavelength tends to be red-shifting. As can be seen from Fig. 9(a), the

Optics EXPRESS

wavelength of interference dip 1 shows the linear red-shifting trend when the temperature is increased from 25°C-55°C, which is identical to the theoretical analysis. Similarly, the wavelength of dip 2 shows the same changing trend as that of dip 1 as the temperature continuously increases [Fig. 9(b)].

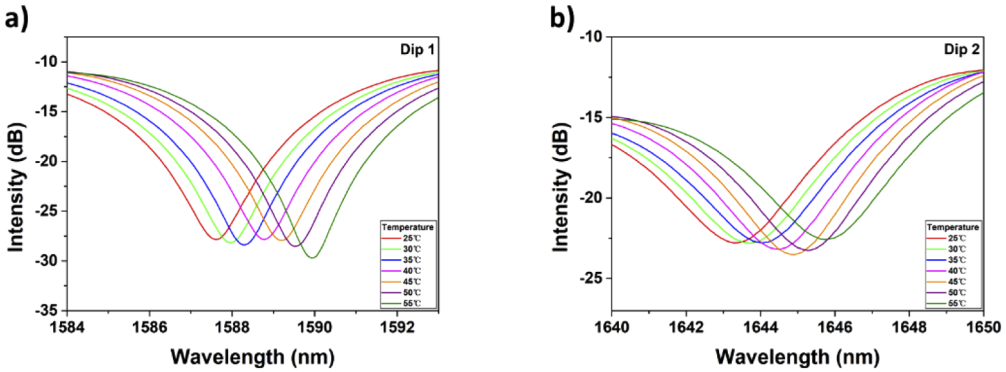

Fig. 9. Interference spectra of (a) dip 1 and (b) dip 2 with different temperatures from 25°C-55°C with an interval of 5°C.

In addition to the central wavelength change of the targeted interference dips, the relationship between the temperature and wavelength shifting is also investigated and illustrated in Fig. 10. To verify the validity of the experimental results, the values of dip wavelength have been recorded and calculated repeatedly by repeating the same experiment four times with the change of temperature (increase and decrease). The error bars are represented by the triangles and the inverted triangles, accordingly. For dip 1, the sensitivity is calculated to be 70 pm/°C and the linearity reaches as high as 0.9992 [Fig. 10(a)]. Meanwhile, the temperature sensitivity of dip 2 is measured to be 72 pm/°C with high linearity of 0.9975. The experimental results indicate a fairly good linearity of both featured interference dips for temperature sensing. Also, the measured temperature sensitivity is relatively high, which is 6 times larger than that reported in [22] and 1.8 times larger than that reported in [23].

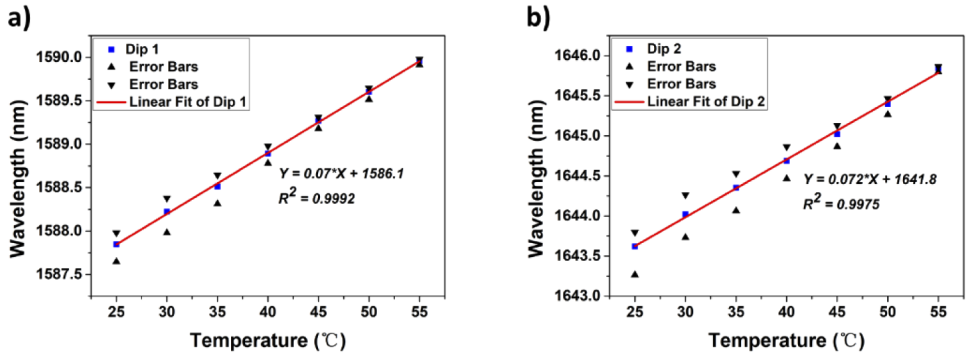

Fig. 10. Mathematical statistics of temperature and wavelength shift of (a) dip 1 and (b) dip 2.

Figure 11 presents the linear relationships between the curvature and the dip wavelength of dip 1 and dip 2. The relations have been recalculated by taking the average values of two slopes obtained with the curvature increasing and decreasing. It is seen that the curvature sensitivity for dip 1 and dip 2 could reach up to -2.27 nm/m^{-1} and -3.58 nm/m^{-1}, respectively.

Optics EXPRESS

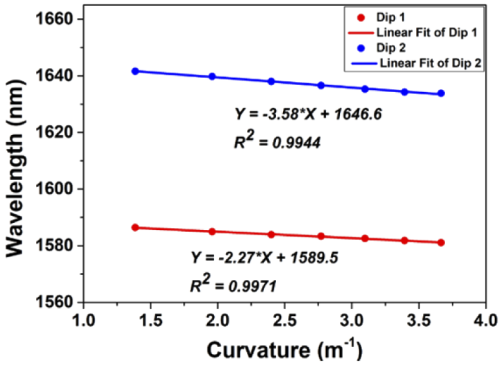

Fig. 11. Linear relationship between curvature and wavelength of dip 1 (red line) and dip 2 (blue line).

Overall, the simultaneous measurement of temperature and curvature can be represented by using the 2×2 matrix based on the linear relationship between the wavelength shift and the variation of temperature and curvature:

$$\begin{bmatrix} \Delta\lambda_1 \\ \Delta\lambda_2 \end{bmatrix} = \begin{bmatrix} 0.07 & -2.27 \\ 0.072 & -3.58 \end{bmatrix} \begin{bmatrix} \Delta T \\ \Delta C \end{bmatrix} \tag{6}$$

where $\Delta\lambda_1$ refers to the wavelength shifting of dip 1 and $\Delta\lambda_2$ represents that of dip 2.

By rearranging the matrix provided in Eq. (6), the temperature and curvature values can be derived with the following transformed matrix:

$$\begin{bmatrix} \Delta T \\ \Delta C \end{bmatrix} = \frac{1}{-0.08716} \begin{bmatrix} -3.58 & 2.27 \\ -0.072 & 0.07 \end{bmatrix} \begin{bmatrix} \Delta\lambda_1 \\ \Delta\lambda_2 \end{bmatrix}. \tag{7}$$

Evidently, with the convenient collection of the wavelength shift of the featured interference dips, the temperature and the curvature change can be easily deduced with our homemade and specially designed MZI sensor. However, it should be noted that the curvature sensing of the MZI fiber sensor is realized in the axis direction of the translation stage. In the near future, the multi-dimensional curvature sensing is expected by improving the structure of RCF-based MZI sensor, such as side-polishing or chemical etching, to meet the requirements of practical applications. In addition, benefiting from the all-fiber structure of the proposed sensor, the high stability can be guaranteed due to optical fiber properties of structural stability and chemical resistance.

4. Conclusion

In conclusion, the RCF-based MZI fiber sensor has been presented in this paper to achieve simultaneous measurement of temperature and curvature with relatively high sensitivities. The theoretical analysis, together with the experimental results has been carried out to predict and evaluate the sensing performance of our homemade MZI fiber sensor. Based on the experimental results, it has been shown that the temperature sensitivity could reach up to 72 pm/°C with the linearity of 0.9975 in the temperature range 25°C-55°C. In the meantime, the maximum sensitivity of curvature sensing is as high as -3.68 nm/m^{-1} with a high adjusted R square value of 0.9959 within the measurement range of 1.3856-3.6661 m^{-1}. Two interference dips around 1587 nm and 1642 nm have been appropriately selected for data analysis. On the basis of the linear

Optics EXPRESS

relationship between the dip wavelength shift and the variation of temperature and curvature, these two physical parameters can be simultaneously extracted by using the 2×2 matrices. Moreover, except for small structures detection, the proposed sensor can also be potentially applied for fixed-point monitoring in large architectural structures benefiting from the optical fiber structure which enables light signals to transmit far away with relatively little loss. The proposed MZI prototype-based curvature sensor is proved to be highly compact, sensitive, reliable, and durable, which is believed to show great potential in a number of applications such as chemical sensing and environmental sensing.

Funding. Guangdong Provincial Pearl River Talents Program (2017BT01X121); Research Grants Council, University Grants Committee (15211317 B-Q60D).

Acknowledgments. W. Yuan designed the experiment, conducted the experiment, analyzed the data, and wrote the manuscript. L. Li helped in building the experimental setups and conducting the experiment. Y. Wang helped with the data analysis. Q. Zhao and C. Yu supported the whole experiment and revised the manuscript.

Disclosures. The authors declare no conflicts of interest.

Data availability. Data underlying the results presented in this paper are not publicly available at this time but may be obtained from the authors upon reasonable request.

References

1. X. Wen, T. Ning, Y. Bai, C. Li, J. Li, and C. Zhang, "Ultrasensitive temperature fiber sensor based on Fabry-Perot interferometer assisted with iron V-groove," Opt. Express **23**(9), 11526–11536 (2015).
2. F. Zhang, X. Xu, J. He, B. Du, and Y. Wang, "Highly sensitive temperature sensor based on a polymer-infiltrated Mach-Zehnder interferometer created in graded index fiber," Opt. Lett. **44**(10), 2466–2469 (2019).
3. T. Paixao, F. Araujo, and P. Antunes, "Highly sensitive fiber optic temperature and strain sensor based on an intrinsic Fabry-Perot interferometer fabricated by a femtosecond laser," Opt. Lett. **44**(19), 4833–4836 (2019).
4. L. Yi and Y. Changyuan, "Highly stretchable hybrid silica/polymer optical fiber sensors for large-strain and high-temperature application," Opt. Express **27**(15), 20107–20116 (2019).
5. S. Dong, B. Dong, C. Yu, and Y. Guo, "High Sensitivity Optical Fiber Curvature Sensor Based on Cascaded Fiber Interferometer," J. Lightwave Technol. **36**(4), 1125–1130 (2018).
6. S. Marrujo-Garcia, I. Hernandez-Romano, M. Torres-Cisneros, D. A. May-Arrioja, V. P. Minkovich, and D. Monzon-Hernandez, "Temperature-independent curvature sensor based on in-fiber Mach-Zehnder interferometer using hollow-core fiber," J. Lightwave Technol. 1 (2020).
7. M. Quan, J. Tian, and Y. Yao, "Ultra-high sensitivity Fabry-Perot interferometer gas refractive index fiber sensor based on photonic crystal fiber and Vernier effect," Opt. Lett. **40**(21), 4891–4894 (2015).
8. V. Ahsani, F. Ahmed, M. B. G. Jun, and C. Bradley, "Tapered Fiber-Optic Mach-Zehnder Interferometer for Ultra-High Sensitivity Measurement of Refractive Index," Sensors **19**(7), 1652 (2019).
9. Q. Zhao, J. Qian, Q. An, and B. Du, "Speedy fabrication of free-standing layer-by-layer multilayer films by using polyelectrolyte complex particles as building blocks," J. Mater. Chem. **19**(44), 8448 (2009).
10. V. Semwal and B. D. Gupta, "Highly sensitive surface plasmon resonance based fiber optic pH sensor utilizing rGO-Pani nanocomposite prepared by in situ method," Sens. Actuators, B **283**, 632–642 (2019).
11. M. Hernaez, B. Acevedo, A. G. Mayes, and S. Melendi-Espina, "High-performance optical fiber humidity sensor based on lossy mode resonance using a nanostructured polyethylenimine and graphene oxide coating," Sens. Actuators, B **286**, 408–414 (2019).
12. W. Yuan, H. Qian, Y. Liu, Z. Wang, and C. Yu, "Highly Sensitive Temperature and Humidity Sensor Based on Carbon Nanotube-Assisted Mismatched Single-Mode Fiber Structure," Micromachines (Basel) **10**(10), 521 (2019).
13. B. Xu, J. Huang, X. Xu, A. Zhou, and L. Ding, "Ultrasensitive NO Gas Sensor Based on the Graphene Oxide-Coated Long-Period Fiber Grating," ACS Appl. Mater. Interfaces **11**(43), 40868–40874 (2019).
14. Q. Yao, G. Ren, K. Xu, L. Zhu, H. Khan, M. Mohiuddin, M. W. Khan, B. Y. Zhang, A. Jannat, F. Haque, S. Z. Reza, Y. Wang, X. Wen, A. Mitchell, and J. Z. Ou, "2D Plasmonic Tungsten Oxide Enabled Ultrasensitive Fiber Optics Gas Sensor," Adv. Opt. Mater. **7**(24), 1901383 (2019).
15. K. Tian, Y. Xin, W. Yang, T. Geng, J. Ren, Y.-X. Fan, G. Farrell, E. Lewis, and P. Wang, "A Curvature Sensor Based on Twisted Single-Mode–Multimode–Single-Mode Hybrid Optical Fiber Structure," J. Lightwave Technol. **35**(9), 1725–1731 (2017).
16. B. Jiang, Z. Bai, C. Wang, Y. Zhao, J. Zhao, L. Zhang, and K. Zhou, "In-Line Mach-Zehnder Interferometer With D-Shaped Fiber Grating for Temperature-Discriminated Directional Curvature Measurement," J. Lightwave Technol. **36**(3), 742–747 (2018).
17. D. Barrera, J. Madrigal, and S. Sales, "Long Period Gratings in Multicore Optical Fibers for Directional Curvature Sensor Implementation," J. Lightwave Technol. **36**(4), 1063–1068 (2018).
18. Y. Wang, D. Richardson, G. Brambilla, X. Feng, M. Petrovich, M. Ding, and Z. Song, "Intensity Measurement Bend Sensors Based on Periodically Tapered Soft Glass Fibers," Opt. Lett. **36**(4), 558–560 (2011).

Optics EXPRESS

19. L. Niu, C.-L. Zhao, H. Gong, Y. Li, and S. Jin, "Curvature sensor based on two cascading abrupt-tapers modal interferometer in single mode fiber," Opt. Commun. **333**, 11–15 (2014).
20. Y. Zhao, F. Xia, and M.-q. Chen, "Curvature sensor based on Mach–Zehnder interferometer with vase-shaped tapers," Sens. Actuators, A **265**, 275–279 (2017).
21. O. Frazao, S. F. O. Silva, J. Viegas, J. M. Baptista, J. L. Santos, J. Kobelke, and K. Schuster, "All Fiber Mach–Zehnder Interferometer Based on Suspended Twin-Core Fiber," IEEE Photonics Technol. Lett. **22**(17), 1300–1302 (2010).
22. B. Sun, Y. Huang, S. Liu, C. Wang, J. He, C. Liao, G. Yin, J. Zhao, Y. Liu, J. Tang, J. Zhou, and Y. Wang, "Asymmetrical in-fiber Mach-Zehnder interferometer for curvature measurement," Opt. Express **23**(11), 14596–14602 (2015).
23. Y.-P. Li, W.-G. Zhang, S. Wang, L. Chen, Y.-X. Zhang, B. Wang, T.-Y. Yan, X.-Y. Li, and W. Hu, "Bending Vector Sensor Based on a Pair of Opposite Tilted Long-Period Fiber Gratings," IEEE Photonics Technol. Lett. **29**(2), 224–227 (2017).